

## Time and Space Variability of Tropical Pacific Wind Stress

STANLEY B. GOLDENBERG<sup>1</sup> AND JAMES J. O'BRIEN

*Departments of Meteorology and Oceanography, Florida State University, Tallahassee, FL 32306*

(Manuscript received 2 May 1980, in final form 4 February 1981)

### ABSTRACT

The results of a spectral analysis of a new, subjectively analyzed data set of tropical Pacific wind stress are presented. The monthly data for the 10-year period, 1961–70, allow a detailed inspection of the distributions of frequency and zonal wavenumber spectra from 29°N to 29°S. In addition, the results obtained using the subjective analysis technique are briefly compared with those obtained using two objective methods.

The frequency spectra vary greatly throughout the tropical Pacific. There also are differences between the spectra for the wind-stress magnitude and its components. The only statistically significant peaks are for the annual and semiannual cycles. Differences between the frequency spectra for the wind-stress magnitude and the wind-stress components are discussed. Plots of the spatial distributions of the power in the annual and semiannual signals are presented and related to seasonal climatological features in the tropical Pacific wind field. Other plots are introduced which show regions of high interannual variability in the area occupied by the Southern Oscillation, and in the central equatorial Pacific. Both of these regions are key areas in the study of El Niño.

Zonal wavenumber spectra are presented as functions of latitude for January, February, etc. The spectra are red, as would be expected.

The outcome of a test for white noise that was performed on the frequency spectra for interannual periods is discussed. According to the data set used in this study, the spectra are indistinguishable from white spectra for interannual periods. However, the results for this type of test are hindered by the short record length available in the data set.

### 1. Introduction

In the meteorological community, there has been an increased interest in the tropics as an aid to improved long-range weather prediction. Oceanographers are building more complicated ocean models for the tropics. In these, the main driving variable is the wind stress. El Niño, a major air-sea interaction event, is believed to be caused by remote forcing in the wind stress over the Pacific Ocean (Wyrski, 1975; Hurlburt *et al.*, 1976; McCreary, 1976; Kindle, 1979). SCOR Working Group 55, "Prediction of El Niño", has established the definition: "El Niño is a massive intrusion of warm water into the eastern equatorial Pacific with positive coastal sea surface temperature anomalies exceeding 2°C as far south as 12°S" (D. W. Stuart, personal communication). This study is an attempt to investigate specific aspects of the time and space variability of the wind stress over the tropical Pacific Ocean.

Willebrand (1978) did one of the most recent studies of the temporal and spatial scales of oceanic winds. He analyzed the quasi-geostrophic wind field

over the Pacific and Atlantic Oceans from 20–65°N. The winds were calculated from synoptic-scale surface pressure data for a 4-year period. He also used actual wind observations from two weather ships. He found that, excluding the annual signal, the spectra of the wind stress are white (i.e., flat) for periods longer than 10 days.

Unfortunately, in the tropics, it is not possible to obtain accurate winds using the pressure field. Early attempts have made use of ship wind observations to study the mean monthly and annual wind distributions (McDonald, 1938; Crowe, 1951a,b; U.S. Navy Hydrographic Office, 1956; Hellerman, 1967). Wyrski and Meyers (1975a,b, 1976) have recently processed 5 million ship wind observations between 30°N and 30°S over the Pacific Ocean for the years, 1900–73. The data were used to create maps of average monthly winds and wind stresses for 2° × 10° latitude-longitude quadrangles. Wyrski and Meyers used the data to study both the seasonal and interannual variability of the Pacific Ocean trade wind field. Barnett (1977a) has used the data to investigate the time and space variability of the trades. Reiter (1978a,b) utilized the data to research the interannual changes in the ocean-atmosphere system.

<sup>1</sup> Present affiliation: Atlantic Oceanographic and Meteorological Laboratories, National Hurricane Research Laboratory, NOAA, Coral Gables, FL 33146.

The wind-stress data for the 10-year period (1961–70) were subjectively analyzed and digitized on a  $2^\circ \times 2^\circ$  latitude-longitude grid. There were three primary motivations for creating a revised data set:

- 1) Obvious errors were contained in the original data set.
- 2) A finer grid was needed to drive coupled atmospheric–ocean models.
- 3) For many of the months, there were regions entirely void of data. Also, there were many  $2^\circ \times 10^\circ$  boxes containing so few observations that the representativeness of the average monthly values was in question.

Barnett (1977a) has analyzed the Wyrтки and Meyers data using empirical orthogonal functions (EOF). For this study, the data also have been analyzed using the method of successive corrections (MSC) employed by Cressman (1959). The results from the subjective analysis are compared with the results that have been obtained using these two objective techniques.

This study uses the digitized data of the subjective analysis to perform a detailed investigation of the distributions of the frequency and wavenumber spectra for the wind stress over the Pacific Ocean. In particular, the power of the semiannual, annual and low-frequency (i.e., interannual) signals is discussed as a function of latitude and longitude. The seasonal variability of the wavenumber spectra is discussed as a function of latitude.

Some ocean climate models incorporate the assumption that the frequency spectra of the wind stress are white for periods longer than the annual (Frankignoul and Müller, 1979). The results are presented of a white noise test that was performed on the spectra for interannual periods.

## 2. The data base

This section will detail the steps that were taken to create the data base of monthly-averaged wind-stress values for the tropical Pacific Ocean on a  $2^\circ$  latitude  $\times$   $2^\circ$  longitude grid for the 10-year period, January 1961–December 1970. Another attempt to provide wind-stress data was by Hellerman (1967), who made use of climatological atlases along with wind-speed frequencies to resolve seasonal wind stress over the world oceans on  $5^\circ$  squares. More recently, Wyrтки and Meyers (1975a,b, 1976) have collected large amounts of ship observations over the tropical Pacific and computed monthly averages of both the wind and wind stress in  $2^\circ$  latitude  $\times$   $10^\circ$  longitude boxes. This latter data set was subjectively analyzed to provide the data base used for this paper.

### a. Original data set

Previous wind-stress distributions, such as Hellerman (1967), were resolved only on  $5^\circ$  squares and by season. One of the limitations with the coarse resolution was the inadequate resolution of north–south gradients. Wyrтки and Meyers (1975a,b, 1976), using a larger collection of observations than previously available (5 million reports), computed bimonthly averages for the period 1900–46, and monthly averages for 1947–73, on a  $2^\circ \times 10^\circ$  latitude–longitude grid.

Those observations with speeds  $> 40 \text{ m s}^{-1}$  during typhoons were not included in the monthly values. The stresses were computed from individual ship wind observations according to

$$\left. \begin{aligned} \tau &= \rho_a C_D W^2 \\ \tau_x &= \rho_a C_D W_x W \\ \tau_y &= \rho_a C_D W_y W \end{aligned} \right\}, \quad (1)$$

where  $\tau$  is the magnitude of the wind stress,  $\rho_a$  the air density,  $C_D$  the drag coefficient and  $W$  the magnitude of the horizontal wind speed defined by  $\mathbf{W} = W_x \hat{i} + W_y \hat{j}$ ,  $W^2 = W_x^2 + W_y^2$ . The subscripts  $x$  and  $y$  refer to the components positive to the east and north, respectively. Constant values were assumed for the drag coefficient,  $C_D = 1.5 \times 10^{-3}$ , and for the air density,  $\rho_a = 1.2 \text{ kg m}^{-3}$ .

### b. Subjective analysis technique

The 10-year period (1961–70) was chosen for the analysis because it is the period with the most consistent data coverage for the years 1947–73. Table 1 shows the monthly data coverage during the decade. Fig. 1 shows the overall average monthly data coverage. The data network was excellent to the north of  $17^\circ\text{N}$ , and good for most of the Northern Hemisphere. However, almost one-fourth of the area in the Southern Hemisphere used for this study was a victim of poor coverage. The quantitative results for those regions are probably unreliable. Fig. 2 shows the actual area covered by the subjective analysis. The analysis included some land areas, even though the original wind stress values were only located over water. The basin was extended to accommodate the approximate land boundaries that are used in ocean models. No additional noise is apparent in the frequency spectra on the boundaries due to this extrapolation. Caution should be exercised, however, when using the extrapolated data.

The analysis was done by drawing separate scalar analyses of the two components of the wind stress  $\tau_x$  and  $\tau_y$ . There were many cases of incorrect or unrepresentative data in the original  $2^\circ \times 10^\circ$  set. In addition, there were boxes totally void of data for

TABLE 1. Number of grid points each month for the period January 1961–December 1970, for which the number of observations (NOBS) was &lt;4 or &gt;30.

Month	Year	NOBS < 4	NOBS > 30	Month	Year	NOBS < 4	NOBS > 30
1	1961	104	106	1	1966	44	143
2	1961	134	95	2	1966	53	131
3	1961	107	126	3	1966	42	141
4	1961	103	100	4	1966	43	143
5	1961	99	102	5	1966	44	135
6	1961	113	96	6	1966	63	130
7	1961	138	65	7	1966	70	129
8	1961	120	87	8	1966	74	149
9	1961	127	55	9	1966	52	138
10	1961	104	90	10	1966	57	139
11	1961	133	83	11	1966	66	148
12	1961	132	93	12	1966	81	139
1	1962	116	103	1	1967	96	131
2	1962	125	83	2	1967	67	147
3	1962	116	105	3	1967	73	139
4	1962	118	98	4	1967	68	138
5	1962	113	92	5	1967	95	133
6	1962	109	97	6	1967	60	122
7	1962	118	91	7	1967	91	124
8	1962	122	80	8	1967	108	138
9	1962	121	71	9	1967	96	134
10	1962	104	89	10	1967	92	135
11	1962	115	89	11	1967	75	132
12	1962	116	84	12	1967	75	133
1	1963	115	91	1	1968	98	137
2	1963	142	64	2	1968	99	132
3	1963	114	91	3	1968	71	134
4	1963	124	83	4	1968	87	143
5	1963	137	87	5	1968	87	123
6	1963	134	75	6	1968	88	130
7	1963	152	69	7	1968	81	126
8	1963	151	67	8	1968	103	136
9	1963	139	80	9	1968	100	131
10	1963	153	86	10	1968	80	145
11	1963	144	74	11	1968	118	118
12	1963	135	95	12	1968	84	127
1	1964	76	124	1	1969	81	135
2	1964	77	123	2	1969	85	140
3	1964	70	125	3	1969	91	154
4	1964	72	106	4	1969	103	130
5	1964	79	126	5	1969	94	137
6	1964	80	98	6	1969	103	127
7	1964	77	116	7	1969	78	142
8	1964	65	108	8	1969	107	130
9	1964	78	101	9	1969	92	127
10	1964	71	124	10	1969	73	139
11	1964	55	128	11	1969	81	140
12	1964	55	140	12	1969	98	139
1	1965	73	141	1	1970	153	120
2	1965	73	114	2	1970	143	115
3	1965	68	152	3	1970	148	130
4	1965	65	141	4	1970	141	116
5	1965	65	142	5	1970	117	126
6	1965	52	128	6	1970	143	118
7	1965	100	131	7	1970	157	111
8	1965	70	143	8	1970	160	107
9	1965	75	125	9	1970	131	112
10	1965	50	133	10	1970	142	108
11	1965	52	152	11	1970	126	113
12	1965	60	140	12	1970	142	107

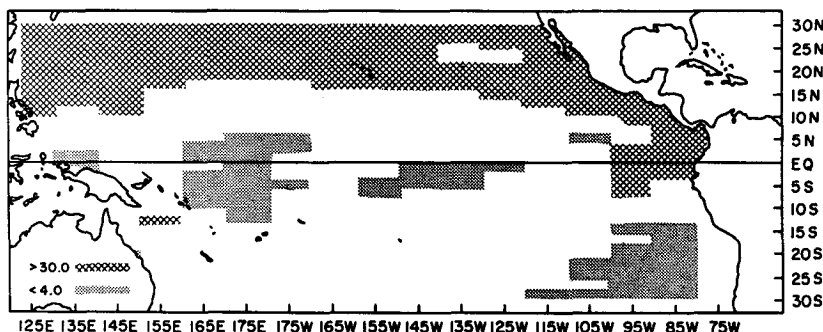


FIG. 1. Areas where the overall average number of monthly observations was <4 or >30 for the 10-year period January 1961–December 1970.

certain months. Standard synoptic techniques were used, such as climatology (McDonald, 1938; Wyrтки and Meyers, 1975a; Hastenrath and Lamb, 1977), continuity, and topography (for boundary regions).

There were several methods for dealing with questionable data. The number of observations (NOBS) in the  $2^\circ \times 10^\circ$  boxes varied from zero to several hundred. Therefore, the representativeness of the wind-stress values as the actual monthly averages also varied considerably. In the analyses, the observations were weighted according to the NOBS for each box for that particular month. There were also obvious errors contained in the original data set. Several occurrences of apparent sign errors were corrected by referring to bimonthly stress vector maps from the original data (Wyrтки and Meyers, 1975b). In addition, the magnitudes of some of the monthly average values were so large that they produced unrealistically strong gradients. These data were either adjusted or discarded.

After the contour maps were drawn, they were digitized using a  $2^\circ \times 2^\circ$  grid. There were several checks made on the digitized data to eliminate errors. Additional details concerning the subjective analysis procedure as well as the complete set of

wind-stress maps are contained in an atlas (O'Brien and Goldenberg, 1981).

The air density  $\rho_a$  is approximately constant within  $30^\circ$  of the equator. It was demonstrated by Willebrand (1978) that the linear stress law (i.e.,  $C_D = \text{constant}$ ) is adequate for a spectral analysis involving periods  $> 10$  days. Therefore, the quantity,  $\rho_a C_D$ , was assumed constant and was not included in the analyses. For the remainder of this paper, the term "wind stress" will refer to the quantities given in (1) without the factor,  $\rho_a C_D$ , i.e.,

$$\left. \begin{aligned} \tau &= \tau_x \hat{i} + \tau_y \hat{j} \\ \tau^2 &= \tau_x^2 + \tau_y^2 \end{aligned} \right\},$$

where  $\tau_x$  and  $\tau_y$ , the zonal and meridional components of the wind stress, respectively, will refer to the quantities

$$\left. \begin{aligned} \tau_x &= W_x W \\ \tau_y &= W_y W \end{aligned} \right\}. \tag{2}$$

*c. Subjective versus objective approach*

After careful consideration of the alternatives, the subjective mapping approach discussed above was

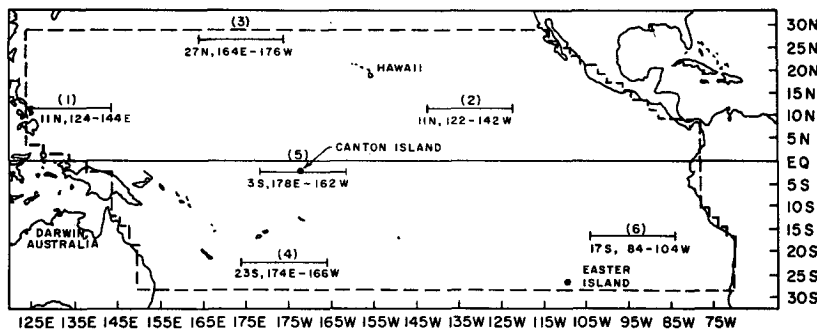


FIG. 2. Subjective analysis "basin" (dashed outline) and locator chart for referenced sites.

chosen to perform the analysis for this study rather than an objective technique. The original monthly  $2^\circ \times 10^\circ$  data also have been analyzed through the use of two objective approaches. Barnett (1977a) used the EOF approach. The present authors analyzed selected months of the original data set using the MSC technique. The results from these methods will be discussed briefly.

The EOF analysis by Barnett covered the years 1950–72. The problem of sparse data coverage was dealt with by using bimonthly,  $4^\circ$  latitude by  $10^\circ$  longitude averages. Some areas of very poor coverage were eliminated. Any remaining voids were filled by “space/time interpolation of missing data using the low-order frequency components of the actual data” (Barnett, 1977a).

The MSC analysis employed the technique developed by Bergthorsson and Döös (1955) and later expanded by Cressman (1959). An elliptical influence radius, based on the ratios of the average gradients in the  $x$  and  $y$  directions, was used for the analysis. The monthly climatological values (Wyrski and Meyers, 1975a) were used as first-guess fields. Also, as shown by Stephens and Polan (1970), it was necessary to filter out all waves after each scan that cannot be resolved by the average station separation, to prevent numerical instability. This analysis was a simple, straightforward attempt to apply MSC to the data. It only covered  $\sim 90\%$  of the area used in the subjective analysis.

There are no major differences between the subjective and the MSC analyses. However, the MSC objective maps contain less detail in the east-west direction because of the filtering described earlier. The disadvantage of the EOF analysis used by Barnett is the smoothing in time and space to obtain uniform data coverage. This results in the loss of detail in the areas with good coverage. The original  $2^\circ$  latitude resolution, which is desirable for computing north-south derivatives (Wyrski and Meyers, 1975a), is reduced to  $4^\circ$  in the EOF analysis. However, the method of filling in the data void areas used by Barnett probably obtains more consistent results than the subjective techniques.

The present subjective data set is the only one at this time on a  $2^\circ \times 2^\circ$  grid. Because no conclusions are made in this study concerning the smaller east-west details, it is doubtful that the use of the MSC approach discussed above, or even a more sophisticated MSC routine, would significantly affect the spectral analysis results.

### 3. Spectral analysis procedure

This section will review the basic spectral techniques that are employed on the data set. The data allow a detailed look at the horizontal distributions of the frequency and wavenumber spectra of the

wind-stress field over the tropical Pacific Ocean. Statistically, the data set is very limited, allowing for only 120 points in time (ten years) and 60–80 equally spaced points in space (i.e., in a latitudinal band). However, this still allows for certain conclusions to be made with reasonable confidence.

The procedure used in this study for the frequency spectra of the stress data is as follows (performed separately for  $\tau$ ,  $\tau_x$  and  $\tau_y$ ):

1) The mean, and in some cases linear trend, are removed.

2) The raw spectral estimates  $S_m$  and the sample variance are computed using the direct Fourier transform method (cf. Jenkins and Watts, 1968). In some cases, these are averaged over a longitude band.

3) The smoothed spectral estimates  $\bar{S}_m$  are obtained using up to two Hanning passes.

The procedure to obtain the wavenumber spectra is identical to the above procedure with the following exceptions:

1) After the linear trend is removed, the series length for each latitude is extended by zeros to 80 points (i.e.,  $160^\circ$  longitude).

2) The spectra computed from the extended series  $S_{m'}$  are adjusted by the factor  $N'/N$ , where  $N'$  is the extended series length of 80 points, and  $N$  is the initial series length. The final  $S_m$ , given by

$$S_m = \frac{N'}{N} S_{m'}, \quad (3)$$

have the property

$$s^2 = \frac{1}{N'\Delta} \sum_{m=1}^{n'} S_m = \frac{1}{N\Delta} \sum_{m=1}^{n'} S_{m'}, \quad (4)$$

where  $n' = N'/2$ ,  $s^2$  is the sample variance and  $\Delta$  the sampling interval (i.e.,  $2^\circ$  of longitude).

3) The spatial spectral estimates are averaged over the ten-year period to produce monthly mean values for each latitude band.

4) Three Hanning passes are used to calculate  $\bar{S}_m$ .

The standard methods for calculating the degrees of freedom, bandwidths and 80% confidence limits for smoothed spectral estimates are given in Jenkins and Watts (1968). It is desirable for the degrees of freedom to be high in order to increase the stability of the spectral estimates. The record lengths for this study are very short. A large number of Hanning passes, which would create the desired degrees of freedom, would also greatly decrease resolution of the smaller details of the spectra.

Instead, an alternate method is used to increase the degrees of freedom while leaving the bandwidth unchanged. For the complete frequency spectra, which will be presented in Section 4b, the spectral

estimates are averaged for 11 adjacent points in the longitudinal direction. This is an application of the ensemble compositing technique. In any time series analysis, the degrees of freedom are determined by the number of observations in the original sample. The original data used to create the subjective analysis were at  $10^\circ$  longitude intervals. The subjective interpolation of the data to  $2^\circ$  longitude intervals cannot be regarded as adding any quantifiable amount of information in terms of degrees of freedom. Upper and lower limits for the degrees of freedom were calculated, along with their respective confidence limits. Let the degrees of freedom for the spectral estimates at each point after the Hanning passes be given by  $\nu_H$ . The upper bound for the degrees of freedom  $\nu_U$  is based on the maximum amount of information that could be contained in the  $2^\circ$  intervals. The lower bound  $\nu_L$  is based on the conservative assumption that no additional information was gained by the subjective analysis that could have increased the degrees of freedom contained in the original  $10^\circ$  longitude values. The upper and lower bounds for  $p$  adjacent points, each with degrees of freedom  $\nu_H$  are given by

$$\nu_L = (\text{INT}[p/6] + 1)\nu_H, \quad \nu_U = p\nu_H, \quad (5)$$

where  $\text{INT}[\ ]$  gives the integer part of the quantity in the brackets. Two Hanning passes are performed on the averaged-frequency spectra before plotting. According to (5),  $\nu_U$  and  $\nu_L$ , the upper and lower bounds of the degrees of freedom, are equal to 80.5 and 14.6, respectively.

Ten-year averages are calculated for the wave-number spectra distributions for January, February, etc. Each of the years is mutually independent. The degrees of freedom is given by  $\nu_U$  in (5), with  $p$  now equal to the number of years used for the averages. Three Hanning passes are performed on the averaged spectra before plotting. For this case, the degrees of freedom is equal to 88.7.

#### 4. Frequency spectra

The characteristics of the bimonthly averages for the period 1947–72, as well as overall seasonal and annual averages have already been discussed in detail for the original data (Wyrтки and Meyers, 1975a,b, 1976). Barnett (1977a) has reviewed the mean distributions for that data set. It is doubtful that the monthly averages in this data set contain significant differences from the original data. Therefore, this section will focus its attention on the distributions of the significant parts of the frequency spectra.

General oceanic circulation models depend on linear forcing by the wind stress. Other models, such as those involving the deepening of the mixed layer, are regulated by a power of the magnitude of the

wind stress. Therefore, this study will look at the spectra for  $\tau$ ,  $\tau_x$  and  $\tau_y$ , separately. In particular, the distributions of the annual, semiannual and total low-frequency variability will be discussed, as well as the distribution of the total variance. Barnett (1977a) has analyzed the original data using the EOF technique. The same analysis has also been performed using the subjective data set (A. Busalacchi, 1979, personal communication). The distribution of energy in the annual cycle, discussed later in this section, agree well with their results for seasonal variability.

For this study, the variance  $s^2$  was computed for the time series at each point of the  $2^\circ \times 2^\circ$  grid. These values are shown for  $\tau$ ,  $\tau_x$  and  $\tau_y$ , in Fig. 3. The time series were then analyzed as described in Section 3, for  $\tau$ ,  $\tau_x$  and  $\tau_y$ , independently. The plots of the spectral density,  $\hat{S}_m$ , are shown in Figs. 4–9 for  $\tau$ ,  $\tau_x$  and  $\tau_y$ , for selected longitudinal bands (see Fig. 2). The spectral estimates are averaged over bands of eleven points in order to improve statistical stability. The upper and lower limits of the degrees of freedom are calculated according to (5). The smoothed spectral estimates  $\hat{S}_m$  for the annual signal are plotted in Fig. 10. The semiannual distributions are shown in Fig. 11.

For certain regions of the tropical Pacific, there may be considerable variability in the 5–20 day band, which could badly alias the 2–6 month frequencies (D. Luther, personal communication). However, this study does not interpret physically the high-frequency tail of the spectra presented here.

There is a great deal of interest in the interannual variability of the wind stress. The long term changes are believed to be related to the anomalous heavy rainfall over the central and western equatorial Pacific (Quinn and Burt, 1970, 1972) as well as to El Niño invasions (Bjerknes, 1966; Quinn, 1974; Wyrтки, 1975; Kindle, 1979; O'Brien *et al.*, 1981). The short record length in this study does not permit sufficient resolution of the interannual peaks (if they exist). Instead, the distribution of the total energy for the signals with periods greater than or equal to 20 months is plotted for  $\tau$ ,  $\tau_x$  and  $\tau_y$  (Fig. 12). The energy for the periods between 12 and 20 months is not used in order to eliminate leakage from the strong annual signal. Two degrees of shading are used rather than contours. A linear trend in the data is often the result of leakage from signals lower than the fundamental frequency. Therefore, the linear trends are not removed for this section, so that all of the interannual variability would be included. The whiteness of the spectra in the low frequencies will be discussed further in Section 6.

The reader should recall from Section 2 that the original data were very sparse in some areas (see Fig. 1). In particular, one should be cautious in drawing conclusions concerning the two large areas of poor

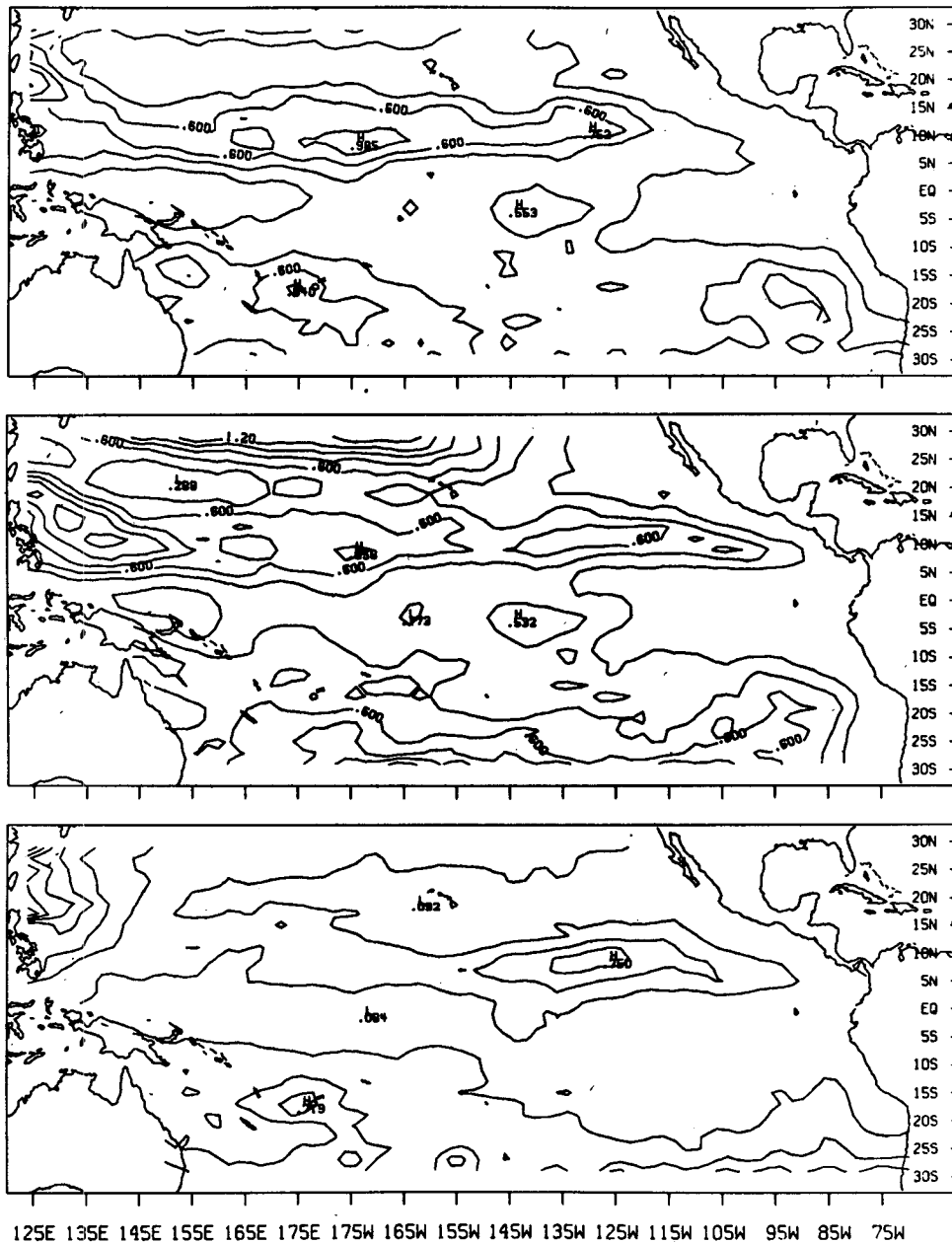


FIG. 3. Spatial distribution of the total variance of the time series for (a)  $\tau$ , (b)  $\tau_x$  and (c)  $\tau_y$ . The linear trends were not removed from the series prior to computing the variances. The contour interval is  $0.2 \text{ m}^3 \text{ s}^{-4} \times 10^9$ .

data coverage which lie near the dateline from about  $5^\circ\text{N}$ – $10^\circ\text{S}$ , and to the west of Chile from  $15$ – $29^\circ\text{S}$ .

*a. Distribution of total variance (Figs. 3a–3c)*

All three charts contain a band of high variance lying between the core regions of the northeast and southeast trades, roughly from  $5$ – $15^\circ\text{N}$ . The band for  $\tau_y$  lies the farthest south, and coincides with the average position for the ITCZ in the eastern

half of the basin. The bands in  $\tau$  and  $\tau_x$  lie slightly farther to the north, stretching almost continuously to the maxima in the northwestern part of the basin, whereas  $\tau_y$  exhibits very low variance from about  $150^\circ\text{W}$  to  $150^\circ\text{E}$ .

There are high variance areas on the northern and southern borders showing up primarily in  $\tau_x$  but also slightly in  $\tau$ . These are due to the intrusion of the westerlies into the subtropics during the winter months.

The other major features of the distribution of variance are located in the northwest and southwest tropical Pacific. These are related to the monsoon circulations of Southeast Asia and Northeast Australia, respectively. Although the total variance of  $\tau_x$  is not high in the latter region, it still exhibits a strong annual signal which will be discussed later.

As expected, all three fields show relatively low variance along the equator. Also, with the exception of the narrow band of high variance in  $\tau_x$ , the easternmost portion of the basin north of 21°S has very low total variance.

Also of interest is the area of high variance to the southwest of Peru, primarily in the  $\tau$  and  $\tau_x$  fields. This feature could be attributed to the variations in the southeast trades north of the center of the subtropical high. However, this is in a region of poor data coverage, so much of the variance there might be due to noise.

*b. Examples of complete spectra (Figs. 4–9)*

The most outstanding feature of the spectra is the prominent annual peak appearing in Figs. 4, 5 and 6. The only other statistically significant peak is the semiannual signal in some of the plots. Excluding the annual and semiannual, the spectra are essentially white. These features, and their differences for plots of the spectra of  $\tau$ ,  $\tau_x$  and  $\tau_y$ , will be discussed briefly for the six plots. The conservative lower limit of the degrees of freedom will be used in interpreting these plots.

In an analysis of the quasi-geostrophic wind field over the northern Atlantic and Pacific Oceans, Willbrand (1978) found the frequency spectra to be essentially white for periods greater than 10 days. For wind data at 52.5°N, 35.5°W, he found the annual signal more pronounced in the spectrum of the stress magnitude than in the spectra for the stress com-

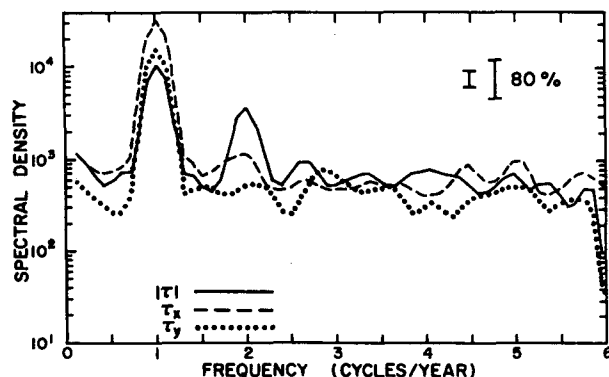


FIG. 4. Power spectra for  $\tau$ ,  $\tau_x$  and  $\tau_y$  for 11°N, 124–144°E. Units for the spectral density are  $(m^4 s^{-4})$  (months). The raw spectra  $S_m$  were smoothed by two Hanning passes. The smaller and larger 80% confidence limits correspond to the upper and lower bounds on calculating  $\nu$  [see (5)].

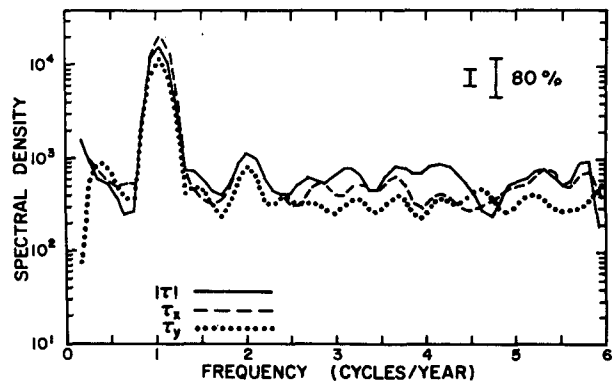


FIG. 5. As in Fig. 4 except for 11°N, 122–142°W.

ponents. This study shows that the relative power of the annual signal in  $\tau$ ,  $\tau_x$  and  $\tau_y$  can vary greatly from region to region.

1) 11°N, 124–144°E (FIG. 4)

This longitudinal band lies in the region dominated by the Southeast Asian monsoon. The annual peak is strongest in the spectrum of  $\tau_x$ , followed closely by the annual peak in  $\tau_y$  and  $\tau$ . There is a significant semiannual peak in the  $\tau$  spectrum, while no well-formed semiannual peak appears in the spectra for  $\tau_x$  or  $\tau_y$ . This feature will be discussed further under annual variability. The rest of the spectra are essentially flat.

2) 11°N, 122–142°W (FIG. 5)

This region is located near the mean position for the ITCZ in the eastern section of the basin. The prominent annual peak is strongest in the  $\tau_x$  spectrum, but it is not significantly different from that for  $\tau$  or  $\tau_y$ . The remainder of the spectra are white, except for a small semiannual peak. The spectra for  $\tau$  and  $\tau_x$  show signs of leakage due to power from very low frequencies (below 0.1 cycles year<sup>-1</sup>). The low-frequency energy in  $\tau_y$  is concentrated around a period of ~3.3 years (although the peak is not statistically significant).

3) 27°N, 164°E–176°W (FIG. 6)

This band lies in the region of the basin affected by the westerlies during the winter months. It is strikingly different from the previous two plots due to the flatness of the stress magnitude spectrum, even though there are pronounced annual and semiannual peaks in the spectra for both of the components. The annual variability in  $\tau_x$  and  $\tau_y$  are out of phase. This leads to the disappearance of most of the variability on the annual scale in  $\tau$ . The  $\tau_y$  spectrum shows a noticeable absence of interannual variability, which is very high for  $\tau_x$  and moderate

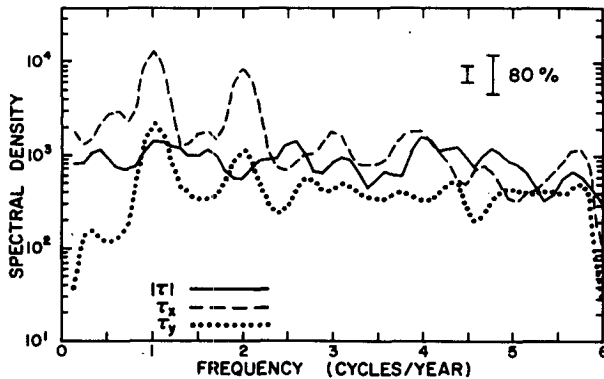


FIG. 6. As in Fig. 4 except for 27°N, 164°E–176°W.

for  $\tau$ . One additional feature is that the  $\tau_x$  spectrum is red, although the slope is not very steep. This feature is also present to a lesser extent in the  $\tau_x$  spectrum for 27°S, 156–176°W (not shown), which corresponds to the intrusion of the westerlies into the Southern Hemisphere subtropics. The redness of the  $\tau_x$  spectra in these two cases suggests that this feature is associated in some way with the seasonal variation of the equatorward extent of the westerlies.

#### 4) 23°S, 174°E–166°W (FIG. 7)

All three of the spectra for this region, which is located in the southwest Pacific, are white. Although there are slight annual peaks in the  $\tau$ ,  $\tau_x$  and  $\tau_y$  spectra, they are not significant relative to the 80% confidence interval. There is a relatively large amount of energy in the interannual band, particularly for the  $\tau$  and  $\tau_x$  spectra. Barnett (1977a) found that the maximum interannual variations in the trades occur primarily in the west and southwest Pacific. The distribution of low frequency energy will be discussed later in this section.

#### 5) 3°S, 178°E–162°W (FIG. 8)

This band is centered on Canton Island in the equatorial Pacific. The spectra for both  $\tau$  and  $\tau_x$  are

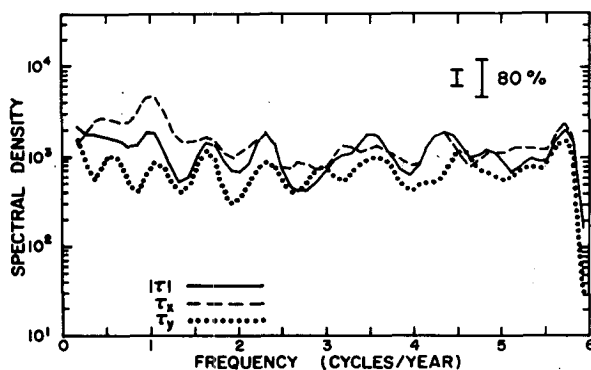


FIG. 7. As in Fig. 4 except for 23°S, 174°E–166°W.

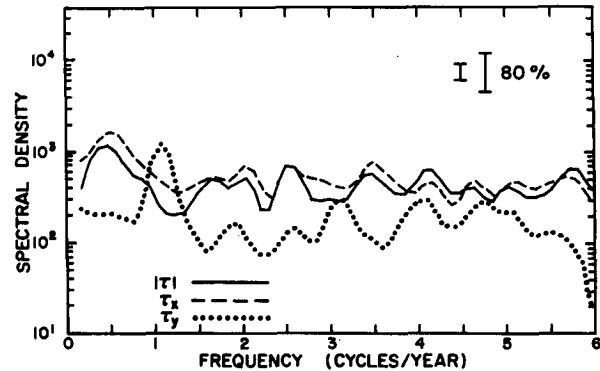


FIG. 8. As in Fig. 4 except for 3°S, 178°E–162°W.

flat. The  $\tau_y$  spectrum contains a significant annual peak. The low-frequency variability in  $\tau$  and  $\tau_x$  is concentrated around a period of about 2.2 to 2.5 years.

#### 6) 17°S, 84–104°W (FIG. 9)

The spectra for this region, which lies just north of the Southern Hemisphere subtropical high, contain no significant annual signal. There is a slight semiannual peak in the spectra for  $\tau$  and  $\tau_x$ , but it is not statistically significant. It is possible that the lack of a significant resolved peak for this band is related to the poor data coverage of this area.

#### c. Distribution of annual variability (Figs. 10a–10c)

It is apparent from the spectra discussed above that the highest variability is in the annual cycle. It is not surprising, therefore, that the distribution of the annual signal is similar to that for the total variance. As was the case for the complete spectra, there are distinct differences in the distribution of the annual signal between the stress magnitude and its two components.

The plots for  $\tau$ ,  $\tau_x$  and  $\tau_y$  all display a band of very high annual energy lying approximately along the

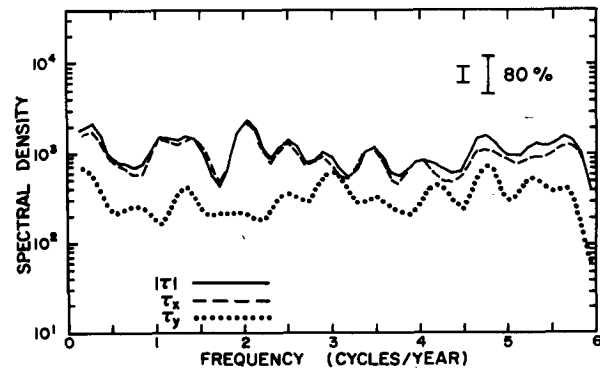


FIG. 9. As in Fig. 4 except for 17°S, 84–104°W.

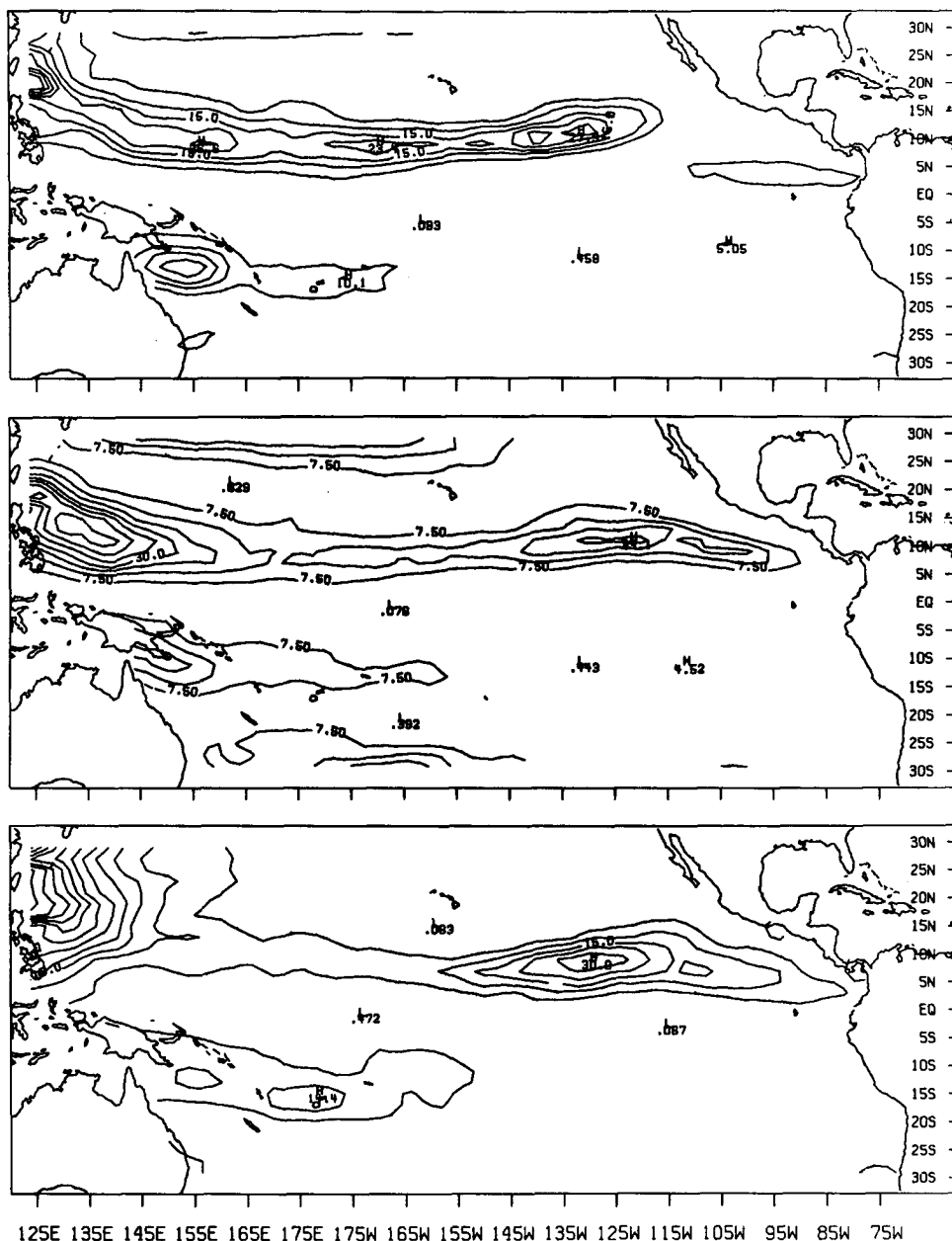


FIG. 10. Spatial distribution of the power in the annual signal for (a)  $\tau$ , (b)  $\tau_x$  and (c)  $\tau_y$ . The raw spectra were smoothed by one Hanning pass. The contour interval for (a) and (c) is  $5 \text{ (m}^4 \text{ s}^{-4}) \text{ (months)} \times 10^3$  and for (b) is  $7.5 \text{ (m}^4 \text{ s}^{-4}) \text{ (months)} \times 10^3$ .

mean position of the ITCZ to the east of the dateline. The maximum for this area in the annual signal for  $\tau_y$  is located along  $9^\circ\text{N}$ , while the eastern maxima for  $\tau$  and  $\tau_x$  are both at  $11^\circ\text{N}$ . The very high values for the annual signal in  $\tau$  and  $\tau_x$  extend across the basin to the west, while the high values in  $\tau_y$  drop off markedly from about  $155^\circ\text{W}$  to  $\sim 145^\circ\text{E}$ . These differences lead to the conclusion that this area of high annual variability in  $\tau_y$  is associated primarily with the seasonal variation of the position of the

ITCZ, whose position fluctuates the most in the eastern Pacific. The high annual signal in  $\tau$  and  $\tau_x$  in this region is associated with the seasonal oscillation in the strength of the northeast trades. Wyrtki and Meyers (1976) demonstrated that the annual variations in the area and strength of the northeast trades are larger than that for the southeast trades.

The plots for  $\tau$ ,  $\tau_x$  and  $\tau_y$  all contain an area of high annual variability in the northwestern corner of the basin. This feature, a product of the monsoon

circulation of Southeast Asia, was discussed in the previous part of this section for Fig. 4. This is an excellent example of a case in which the annual signal is larger for the components than for the stress magnitude. Because of the winter and summer monsoons, the mean flow at 11°N, 125°E, is from the northeast from November through April, and from the southwest from July through October (Wyrтки and Meyers, 1975a). This results in a large annual variation in the wind components. Although the wind components exhibit a strong annual signal, some of this annual variability might show up as a strong semiannual signal in the spectrum of the wind speed. Such is the case demonstrated in Fig. 4. The spectra for  $\tau_x$  and  $\tau_y$  both contain a large annual peak, but no semiannual peak. The spectrum for  $\tau$  displays a smaller annual peak, but also a pronounced semiannual peak. This is an important consideration with looking at the oceanic response to the winds. The deepening of the mixed layer in the ocean responds to the magnitude of the wind stress. Therefore, in some cases a portion of the annual variability in the wind field can show up as semiannual variability in the depth of the mixed layer.

The maxima off northeast Australia are consequences of the Australian monsoon. The areas of high power for the annual signal in  $\tau_x$  (and showing up slightly in  $\tau$ ) in the extreme north and south of the basin are the result of the wintertime intrusion of the westerlies into the subtropics of the Northern and Southern Hemispheres, respectively. Both of these features have been discussed previously in this section with respect to the distribution of total variance.

The time amplitude functions for the  $U_2$  and  $V_2$  eigenvectors of the EOF analyses performed by Barnett (1977a) and Busalacchi (1979, personal communication) are modulated seasonal signals. The eigenvector patterns and the major features of the distribution of the annual variability in this study are very similar. The differences are probably due to the coarser spatial resolution employed in the EOF analyses. Also, Barnett's analysis covered a longer time span, 1950–72, than the subjectively analyzed data.

#### *d. Distribution of semiannual variability (Figs. 11a–11c)*

There are five areas displaying high semiannual energy. The semiannual variability of the region which lies off the Philippines and the region to the west of Peru have both been discussed earlier in this section.

The most prominent feature is the region of very high semiannual energy in Fig. 11b to the north of 23°N in the western half of the basin. The complete spectra and the high annual signal have been ana-

lyzed previously in this section. The spectra showed a significant semiannual peak, plus small peaks at 3 and 4 cycles per year (see Fig. 6). The monthly average values for  $\tau_x$  are very high in winter, yielding a non-sinusoidal annual variation. This results in the ringing of the harmonics of the annual frequency.

The region of high semiannual energy in  $\tau$  centered at 21°N, 162°E, is a feature resulting from true 6-month variability. The seasonal shifting of the subtropical high causes the belt of strongest trades at 162°E to cross this latitude twice annually. This results in maxima for  $\tau$  and  $\tau_x$  to occur around April and October (Wyrтки and Meyers, 1975a). The spectra for the band at 21°N, 154–174°E (not shown), contain a significant semiannual peak in  $\tau$  and  $\tau_x$ . There is no statistically significant six-month peak for  $\tau_y$ . (The spectrum for  $\tau_y$  displays a pronounced annual peak because as the subtropical high moves north, the flow becomes southeast. This produces a large yearly fluctuation about zero.)

The  $\tau_y$  spectra (not shown) for the area in the southeast corner of the basin does not exhibit a significant semiannual peak. The relatively high energy there in the semiannual signal could be a product of increased noise due to poor data coverage and extrapolation. This would be in agreement with the study by Hsu and Wallace (1976), which shows a minimum in semiannual pressure variation for that region.

#### *e. Distribution of interannual variability (Figs. 12a–12c)*

The most interesting feature is the band of high energy stretching almost continuously across the basin from Chile to Australia. It appears in the distributions for  $\tau$ ,  $\tau_x$  and  $\tau_y$ , and is strongest to the west of 120°W. The Southern Oscillation Index, the difference in sea level atmospheric pressure between Easter Island and Darwin, Australia, has been used as a method for predicting anomalous equatorial Pacific events such as occurrences of El Niño invasions (Quinn, 1974; Wyrтки *et al.*, 1976). This study supports the idea that the region exhibits high interannual variability.

Another area of high power in the low-frequency band lies just north of the equator in the central Pacific for  $\tau$ ,  $\tau_x$  and  $\tau_y$ . This result supports the theory for El Niño developed by Wyrтки (1975). He stated that, prior to the occurrence of El Niño, there is an increase in the southeast trades over the central equatorial Pacific. This produces a pileup of water in the western half of the Pacific basin. When the trades subsequently relax, the accumulated water will move back toward the east in the form of a downwelling, equatorially trapped Kelvin wave (Hurlburt *et al.*, 1976; McCreary, 1976). The high-

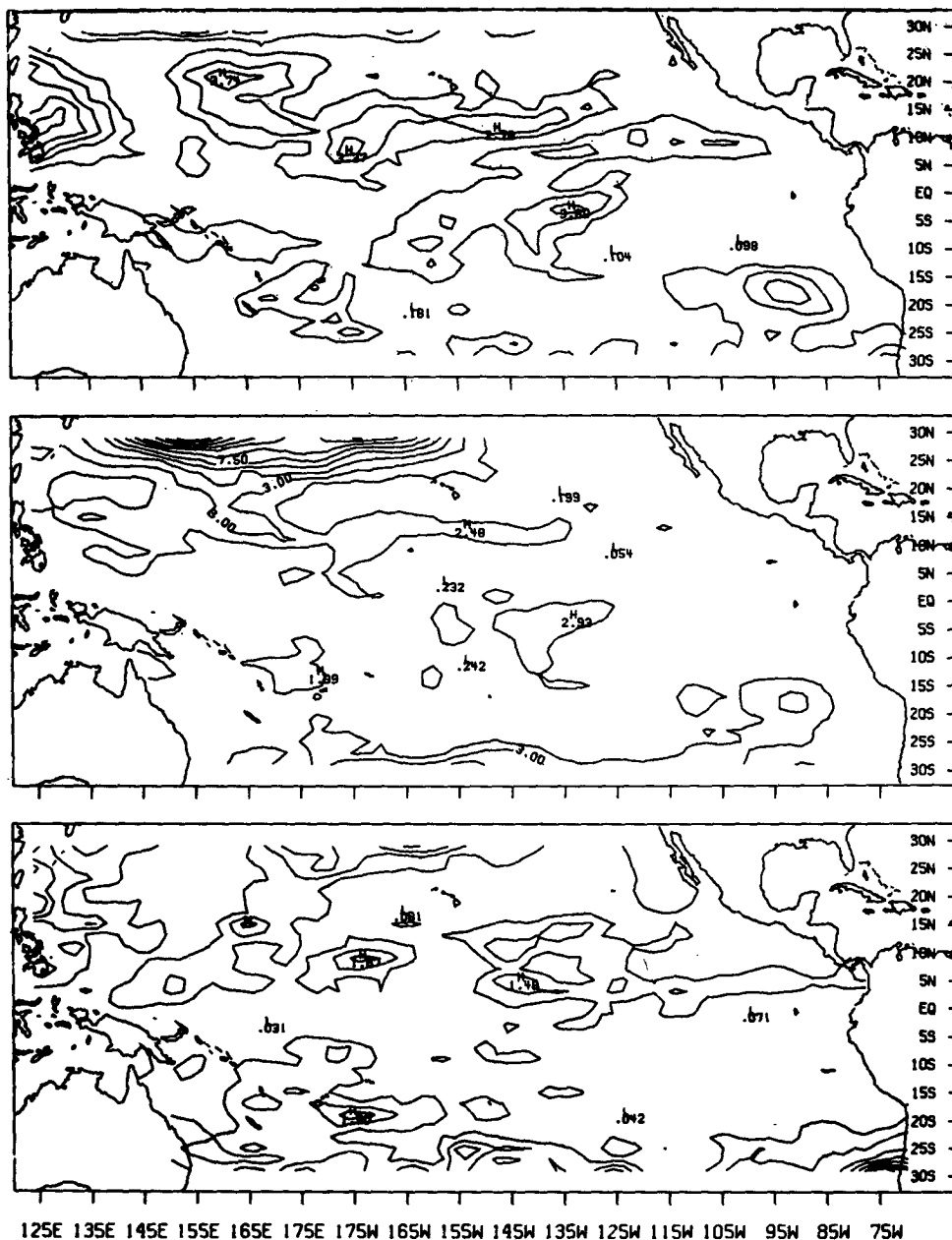


FIG. 11. Spatial distribution of the power in the semiannual (six month) signal for (a)  $\tau$ , (b)  $\tau_x$  and (c)  $\tau_y$ . The raw spectra were smoothed by two Hanning passes. The contour interval is  $1 \text{ (m}^2 \text{ s}^{-2}) \text{ (months)} \times 10^3$  for (a),  $1.5 \text{ (m}^2 \text{ s}^{-2}) \text{ (months)} \times 10^3$  for (b) and  $0.5 \text{ (m}^2 \text{ s}^{-2}) \text{ (months)} \times 10^3$  for (c).

energy areas west of  $160^\circ\text{E}$  are in the Asian monsoon area and also may contribute to El Niño events (O'Brien *et al.*, 1981).

The other area of high energy lies poleward of  $21^\circ\text{N}$  in the central Pacific. It is the result of the interannual variability of the degree of southward intrusion and intensity of the westerlies during the winter months.

Of particular importance is the absence of high variability along most of the western coast of North

and South America. This is in agreement with the theory that El Niño events are not the result of local wind changes, but are instead caused by remote forcing in the central and western Pacific (Wyrski, 1975; Barnett, 1977b; Kindle, 1979; O'Brien, 1979). The area of high variability in  $\tau$ ,  $\tau_x$  and  $\tau_y$ , directly west of Chile, lies in a region of very poor data coverage. The band of low variability along the coast, south of the equator, is in an area of adequate data coverage. North of the equator, the coast is

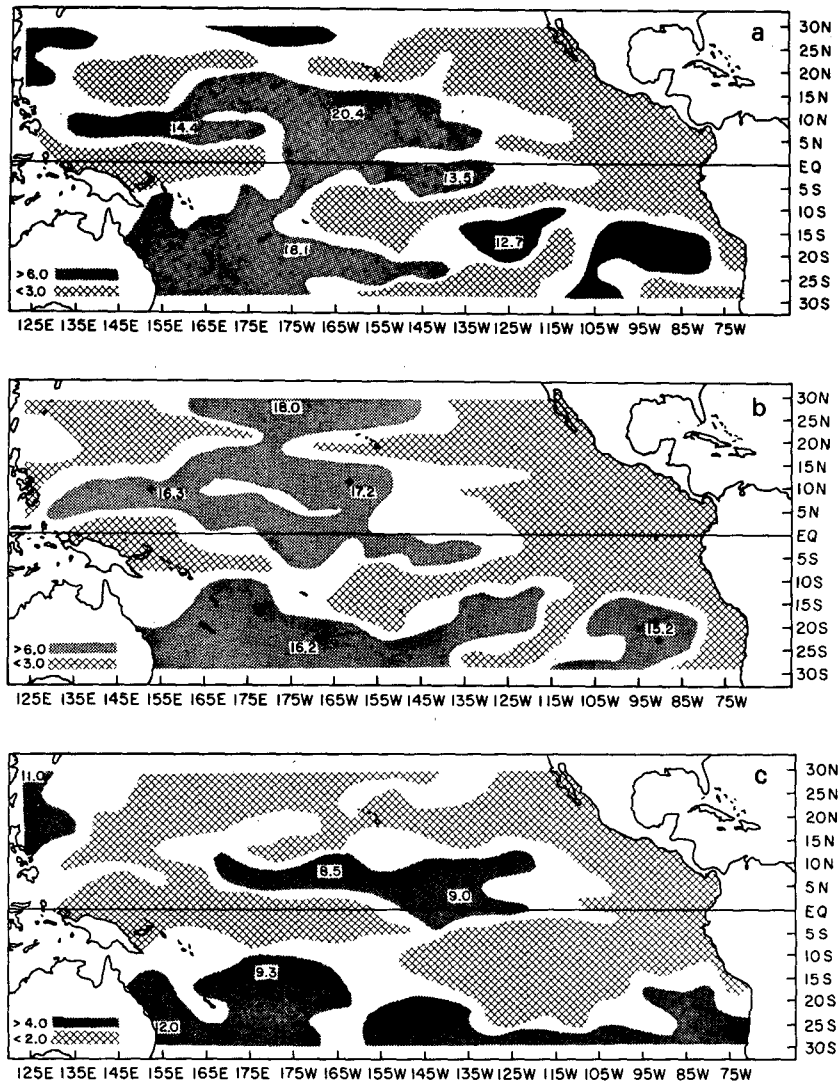


FIG. 12. Distribution of the total low-frequency energy for (a)  $\tau$ , (b)  $\tau_x$  and (c)  $\tau_y$ . Values for several selected maxima are given. The units are  $(\text{m}^4 \text{s}^{-4}) (\text{months}) \times 10^3$ .

typified by greater than 10 observations per month on the average.

### 5. Zonal wavenumber spectra

This section will discuss the wavenumber spectra obtained by performing the analysis described in Section 3. The series length is  $160^\circ$  of longitude (i.e., 80 points) for all latitudes. The linear trends were removed to decrease the possibility of leakage from wavenumbers lower than those resolvable by the basin width. The analysis was only done for the stress magnitude. This gives the distribution in wavenumber space of the kinetic energy. Initially, the log of the power spectra  $\bar{S}_m$  was plotted versus global wavenumber (GWN) and latitude for each month (not shown). The plots of  $\log \bar{S}_m$  demon-

strated the expected red spectra with no statistically significant peaks for all 12 months. However, the slopes vary with latitude and month. More than 95% of the spatial variance is associated with  $\text{GWN} < 18$ . On the average, this is the highest GWN that could be resolved by the original data (i.e.,  $20^\circ$  of longitude).

The wavenumber times the power spectrum (i.e.,  $m\bar{S}_m$ ) was plotted as a function of latitude on a logarithmic wavenumber scale for each month. Figs. 13 and 14 give the results for February and August, respectively, which are typical values for winter and summer. Space does not permit showing all 12 months. The GWN is shown opposite the wavenumber on both plots.

One of the most interesting features of the plots for  $m\bar{S}_m$  (i.e., Figs. 13 and 14) is that they are

latitudinally coherent. This is in spite of the fact that a subjective analysis technique was used to create the data set, and that the spectral analysis was performed separately for each latitude band. Other features are the large peaks which appear in Fig. 13 at 29 and 15°N. There are several small peaks in the Southern Hemisphere. The peaks signify that the spatial variability is concentrated in certain GWN bands. For the Northern Hemisphere peaks, the variance is concentrated between GWN 3–12. The peak at 29°N obviously is a result of the variance due to the wintertime westerlies. The peak is present from December to March, and is the strongest in February. The maximum which is located at 15°N during February also varies throughout the year. During some months, it spreads over 5° of latitude, or splits into two maxima. The center of the peak varies from GWN 3.5–7, favoring lower GWN in spring and summer. The feature is probably the result of a combination of effects such as the Southeast Asian and Central American monsoons (Wyrtki and Meyers, 1976), the core of maximum winds for the northeast trades, and the ITCZ. Tropical disturbances might also affect the results here. However, the observations of strong winds during hurricanes were eliminated when the data was originally processed (Wyrtki and Meyers, 1975a).

The hemispheric differences might be due to poor data coverage, as well as to the differences in seasons. Also, there are major climatological asymmetries between the wind fields of the North and South Pacific. There are two large peaks in the Southern Hemisphere wavenumber spectra for August (Fig. 14). The peak centered at 20°S and GWN 7 is due to the strong southeast winds east of Australia and the strong southeast trades just west of Chile and Peru (cf. O'Brien and Goldenberg,

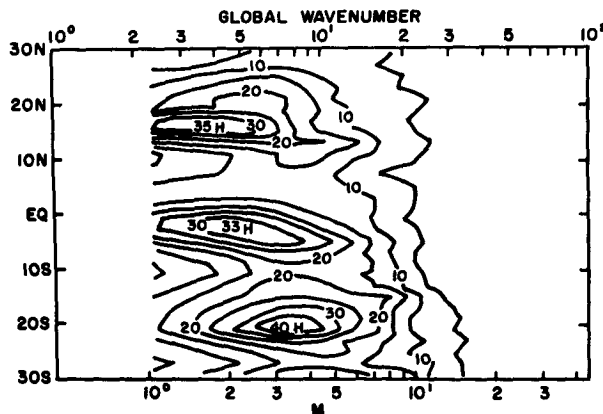


FIG. 14. As in Fig. 13 except for August.

1981). A similar peak also appears in most of the other months. The peak centered at 3°S and GWN 5 is caused by the combination of light winds near New Guinea and the core of maximum southeast trades in the eastern Pacific. August is the only month which exhibits this peak. During the analysis period (1961–70), August typically had one of the worst data coverages (see Table 1). Almost half of the band from 0–5°S had an overall average of less than four observations per month (see Fig. 1). It is likely that the peak has been exaggerated by effects related to the data coverage.

**6. Are the wind-stress spectra white for low frequencies?**

This section will attempt to answer the question of whether or not the wind-stress frequency spectra are white for interannual periods. This is an important problem, because some ocean climate models depend on the supposition that the spectra are white for low frequencies (Frankignoul and Müller, 1979). The frequency spectra for the spatially averaged zonal wind stress of the northeast and southeast trades for 1948–72, were calculated by Wyrtki and Meyers (1976). Their results show no significant peak for interannual periods. However, the coherency between the trades increases above the 95% confidence limit for the lowest frequencies. It is obvious that the significance of the results of the test used in this study will be inhibited by the even shorter record length of 10 years. However, as in the discussion in Section 4 of the total low-frequency energy, the results reveal interesting distributions, even though their statistical reliability is small.

The Kolmogorov–Smirnov goodness-of-fit test (K–S test) is used at each point to evaluate the null hypothesis that the spectrum for low frequencies is white (Jenkins and Watts, 1969). The test uses the integrated spectrum as a cumulative dis-

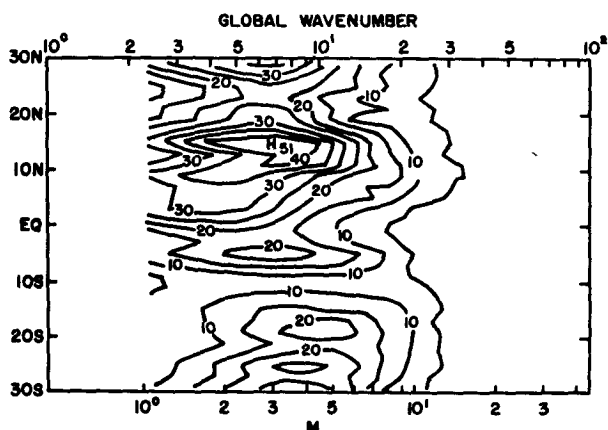


FIG. 13. Wavenumber times wavenumber power spectrum (i.e.,  $m^4 s^{-4}$ ) versus latitude for February. The averaged spectral estimates were smoothed by three Hanning passes. The first harmonic (GWN = 2.25) represents a wavelength of 160° of longitude. The contour interval is 5 ( $m^4 s^{-4}$ ) (deg)  $\times 10^3$ .

tribution function. The maximum absolute deviation from the theoretical distribution is called  $D_{\max}$ . This is compared to a critical value  $D_{\text{crit}}$  for a particular level of significance. The significance level for this study was chosen to be 20%. Spectral estimates for periods greater than or equal to 120/7 months (the first seven harmonics) were used to construct the integrated spectrum. In this type of test, the last estimate, i.e., the highest frequency used, does not affect the results. Therefore, just as for the discussion of the total low-frequency energy in Section 4, only the spectral estimates for periods  $\geq 20$  months are actually being tested for whiteness. For the purpose of this test, the linear trend was removed from the time series at each point before the spectral estimates were computed.

The test was performed on the unsmoothed, low-frequency spectra for  $\tau$ ,  $\tau_x$  and  $\tau_y$ . The value used for  $D_{\text{crit}}$  was 0.410 (Ostle, 1963). However, the resultant number of points which failed the test for the hypothesis appeared to be too small. Less than 12% of the points tested for  $\tau$ ,  $\tau_x$  and  $\tau_y$  failed the test. Even if the spectral estimates were from a white noise process,  $\sim 20\%$  of the points should have failed the test because of the 20% significance level. In order to verify this, random  $\chi^2$  variables with two degrees of freedom were generated. If  $0 < x < 1$  is a random number with a uniform distribution function, then  $\chi^2 = -2 \log x$  is a chi-square variable with 2 degrees of freedom. The random variables were used to simulate the raw spectral estimates of a white noise process. When the same K-S test was performed on the random data, only  $\sim 13\%$  of the points failed the null hypothesis. Thus, either the values from the table are incorrect for this application, or the sample size of seven estimates at each point is too small for the type of test being used.

A new critical value was calculated by first creating a probability density distribution from the values of  $D_{\max}$  calculated above when the randomly generated  $\chi^2$  variables were used. The K-S test was run for 2155 points. This was a sufficient number for a good probability density distribution. The 20% level was found to be associated with  $D_{\text{crit}} = 0.373$ . The K-S test was then repeated on the low frequency spectra for  $\tau$ ,  $\tau_x$  and  $\tau_y$ , with the new empirical value for  $D_{\text{crit}}$ . Of the 2155 points, 19% failed the null hypothesis for  $\tau$ , and 18% of the points failed for both  $\tau_x$  and  $\tau_y$ . These values are approximately what would be expected if the process was indeed white noise. However, the spatial distributions of the points which failed the K-S test are of interest and deserve further discussion.

Fig. 15 shows the results for  $\tau$  and for the randomly generated  $\chi^2$  variables. As would be expected, the points at which the  $\chi^2$  variables are significant appear to be random. There are some

areas for the  $\tau$  distribution that are more densely covered than others. These include:

- 1) The region in the eastern half of the South Pacific from about 11–23°S. This is a section of the region where the Southern Oscillation index is measured (Quinn, 1974; Wyrski *et al.*, 1976). It should be noted that part of this region is an area of poor data coverage (see Fig. 1).
- 2) The region in the North Pacific from about 140–178°E. This area is associated with the Southeast Asian monsoon circulation.
- 3) The area surrounding the average position of the ITCZ ( $\sim 10^\circ\text{N}$ ) in the central North Pacific.

In addition, the distribution for  $\tau_x$  (not shown) includes a region of dense coverage north of 23°N from about 155°E–170°W. This would be associated with the interannual variation of the wintertime westerlies discussed in Section 4. The distribution for  $\tau_y$  (not shown) contains one additional area, just off the east coast of Australia. The density of the patterns can be deceiving, however. This is because, as discussed previously in Sections 3 and 4, the neighboring points are not truly independent. Five longitudinal points were created for every point of the original data. Thus, east–west bands of up to five points should not be considered significant. The above discussion does not apply to adjacent points in the north–south direction.

The tentative conclusion for the results of this section is that the wind stress spectra are white for low frequencies. However, the patterns of the points which fail the test are intriguing and should be checked with longer data sets.

## 7. Summary and conclusions

Ship wind observations, averaged month by month for  $2^\circ \times 10^\circ$  latitude–longitude boxes by Wyrski and Meyers (1975a,b, 1976), are subjectively analyzed to provide monthly maps of wind stress for the decade 1961–70 on a  $2^\circ \times 2^\circ$  grid over the tropical Pacific. Frequency and seasonal zonal wavenumber spectra are calculated. The results reveal that the frequency spectra vary greatly from region to region. Only the annual and semiannual peaks are statistically significant using 80% confidence limits.

The subjective analysis techniques used for this study are briefly compared with two objective analysis techniques: the method of empirical orthogonal functions (Barnett, 1977a) and the method of successive corrections. The spatial smoothing is greater in both of the objective methods than for the subjective analysis. The latitudinal smoothing used in the EOF approach could have the effect of decreasing the accuracy of north–south derivatives.

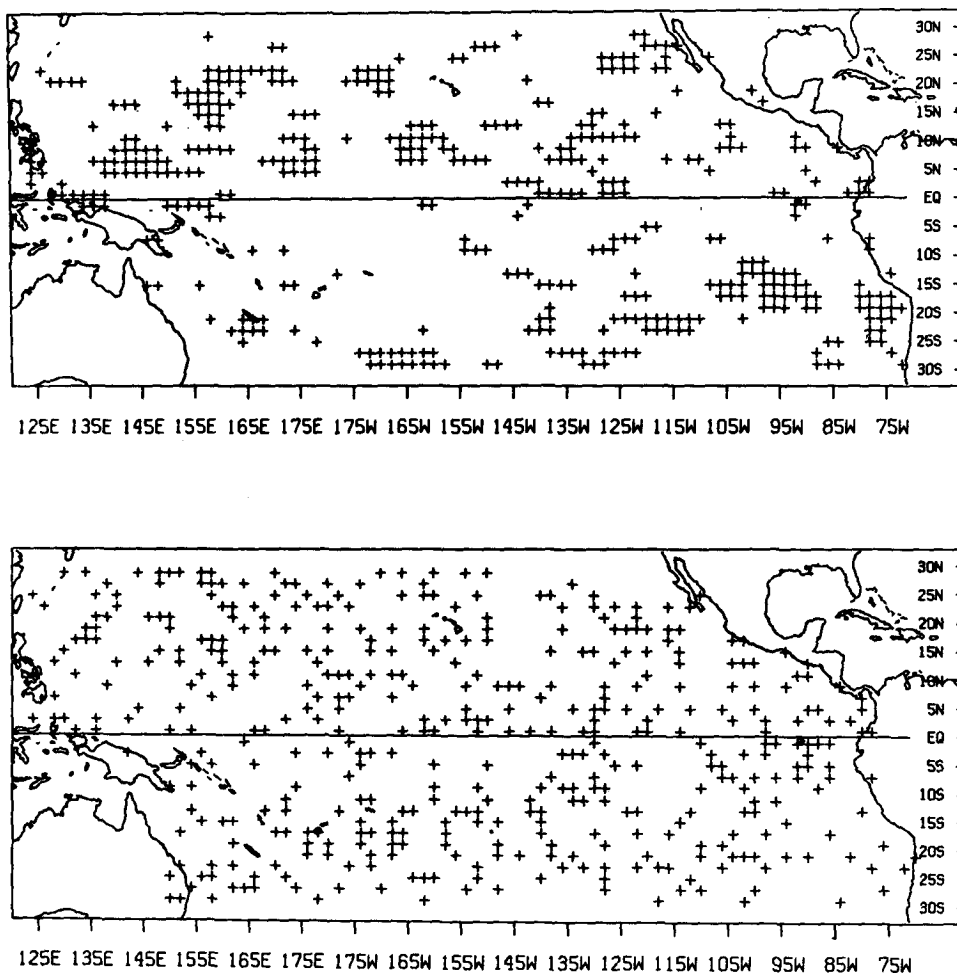


FIG. 15. Results of the K-S test for white noise for (a)  $\tau$  and (b)  $\chi^2$  r.v. with 2 df. Points which failed the null hypothesis at the 20% significance level are indicated by plus signs.

The other differences are in the techniques used to fill in the data void regions. It is doubtful that any of these variations would contribute to significant differences in the spectral analysis of the present study.

Frequency spectra of the wind stress allow an examination of the time scales 2 months to 10 years. The spectra vary greatly between the wind-stress magnitude  $\tau$  and the wind-stress components  $\tau_x$  and  $\tau_y$ . The spectra for a large portion of the tropical Pacific display a pronounced annual signal, which is typically strongest for the zonal component  $\tau_x$ . It is demonstrated how the annual variability for  $\tau_x$  and  $\tau_y$  can be folded into the semiannual time scale in  $\tau$ . These differences between the wind-stress magnitude and the components can be important when looking at the oceanic response to the winds for different types of ocean models.

Distributions for annual and semiannual variability clearly show the well-known climatological features:

the monsoon circulations of Southeast Asia and North Australia, wintertime intrusion of the west-lies into the subtropical Pacific, seasonal variations in the position of the ITCZ and the oscillation in the strength of the northeast trades.

The 10-year record length of the present study is too short to accurately resolve interannual variability. As an alternative, the distribution of the total energy for all periods 20 months and longer is plotted. There are three areas of high interannual variability: a band stretching from Chile to Australia, a region over the central equatorial Pacific and a region poleward of 21°N in the central Pacific. The first area is located in the region where the Southern Oscillation Index (SOI) is measured. The SOI has been used to predict El Niño occurrences (Quinn, 1974; Wyrski *et al.*, 1976). The second area is believed to be the key area in the remote forcing mechanism which causes El Niño. The result for this area, along with the very low

interannual variability found along the western coast of South America, are further confirmations of the theory of El Niño, originally developed by Wyrski (1975). The third area is associated with interannual variability in the intensity of the westerlies which influence the subtropics during the winter months.

The monthly zonal wavenumber spectra are red, as expected. The spatial variability is concentrated in global wavenumbers 3–12, particularly in the latitudes influenced by wintertime westerlies, containing the ITCZ or the cores of the maximum trade winds. More than 95% of the variance is contained in the spatial scales resolvable by the original data (i.e., 20° of longitude). Additional research could study the frequency–wavenumber spectra to investigate the distribution of spatial atmospheric variability as a function of frequency.

The last part of the present study employs the Kolmogorov–Smirnov goodness-of-fit test to examine the low frequency spectra for whiteness. A new empirical critical value is used for the test at the 20% significance level. The results confirm earlier studies that the wind spectra are white for interannual periods. However, the regions where points failed the test for white noise are of special interest, such as the area surrounding the average position of the ITCZ in the central North Pacific. It would be desirable to investigate the low-frequency spectra further when longer data sets are made available.

The purpose of this study is to provide a better insight into the distribution of time and space variability of the wind stress. It is hoped that the results can be used to further investigate the oceanic response to the seasonal and interannual atmospheric forcing. With a data set such as this, there are considerably more analyses that could be performed. The data are available for other investigators.

*Acknowledgments.* The authors would like to thank Drs. Charles Jordan, Noel LaSeur, Duane Meeter, Lloyd Shapiro and Jesse Stephens for their helpful discussions and suggestions. We also appreciate the technical help provided by George Heburn, Monty Peffley, Dale Hawkins and Tony Busalacchi.

We are deeply grateful to the many people who helped with the tedious task of creating the data base that was used for this study. In particular, we wish to thank James Allsopp and Robert Davy for their excellent work. We wish to acknowledge Drs. Klaus Wyrski and Gary Meyers for processing the original ship wind observations and for making those results available for use in this study.

In addition, we would like to thank Susan Finney for typing both the draft copies and the final version of the thesis.

This research is derived from an M.S. thesis by

S. B. Goldenberg submitted to the Florida State University, Department of Meteorology. Support was provided by the Division of Atmospheric Sciences, National Science Foundation, under Grant ATM7920485, the CUEA Project of IDOE, NSF and the Office of Naval Research. Computations were performed on the CDC Cyber 73 and Cyber 74 at the Florida State University Computing Center.

This research is contribution No. 157 of the Geophysical Fluid Dynamics Institute, Florida State University, and Contribution No. 2 of PEQUOD.

#### REFERENCES

- Barnett, T. P., 1977a: The principal time and space scales of the Pacific trade wind fields. *J. Atmos. Sci.*, **34**, 221–236.
- , 1977b: An attempt to verify some theories of El Niño. *J. Phys. Oceanogr.*, **7**, 633–647.
- Bergthorsson, P., and B. Döös, 1955: Numerical weather-map analysis. *Tellus*, **7**, 329–340.
- Bjerknes, J., 1966: Survey of El Niño 1957–58 in its relation to tropical Pacific meteorology. *Inter-Amer. Trop. Tuna Comm. Bull.*, **12**, 62 pp.
- Crowe, P. R., 1951a: The trade wind circulation of the world. *Inst. Brit. Geogr. Trans. Pap.*, No. 15, 39–56.
- , 1951b: The seasonal variation in the strength of the trades. *Inst. Brit. Geogr. Trans. Pap.*, No. 16, 25–47.
- Cressman, G. P., 1959: An operational objective analysis system. *Mon. Wea. Rev.*, **87**, 367–374.
- Frankignoul, C., and P. Müller, 1979: Quasi-geostrophic response of an infinite  $\beta$ -plane ocean to stochastic forcing by the atmosphere. *J. Phys. Oceanogr.*, **9**, 104–127.
- Hastenrath, S., and P. Lamb, 1977: *Climatic Atlas of the Tropical Atlantic and Eastern Pacific Oceans*. The University of Wisconsin Press, 15 pp.
- Hellerman, S., 1967: An updated estimate of the wind stress on the world ocean. *Mon. Wea. Rev.*, **95**, 607–626.
- Hsu, C.-P. F., and J. M. Wallace, 1976: The global distribution of the annual and semiannual cycles in sea level pressure. *Mon. Wea. Rev.*, **104**, 1597–1601.
- Hurlburt, H. E., J. C. Kindle and J. J. O'Brien, 1976: A numerical simulation of the onset of El Niño. *J. Phys. Oceanogr.*, **6**, 621–631.
- Jenkins, G. M., and D. G. Watts, 1968: *Spectral Analysis and Its Applications*. Holden-Day, 543 pp. (see Chaps. 6 & 7).
- Kindle, J. C., 1979: Equatorial Pacific Ocean variability—seasonal and El Niño time scales. Ph.D. thesis, Florida State University, 148 pp.
- McCreary, J., 1976: Eastern tropical ocean response to changing wind systems with application to El Niño. *J. Phys. Oceanogr.*, **6**, 632–645.
- McDonald, W., 1938: *Atlas of Climate Maps of the Ocean*. U.S. Weather Bureau Paper No. 1247, 130 pp.
- O'Brien, J. J., 1979: Equatorial oceanography. *Rev. Geophys. Space Phys.*, **17**, 1569–1575.
- , A. Busalacchi and J. Kindle, 1981: Ocean Models of El Niño. *Resource Management and Environmental Uncertainty: Lessons from Coastal Upwelling Fisheries*, M. Glantz and J. D. Thompson, Eds., Wiley-Interscience.
- , and S. B. Goldenberg, 1981: *Atlas of Tropical Pacific Wind Climatology, 1961–1970*. Florida State University, Tallahassee, 200 pp. (in press).
- Ostle, B., 1963: *Statistics in Research*. The Iowa State University Press, 585 pp.
- Quinn, W. H., 1974: Monitoring and predicting El Niño invasions. *J. Appl. Meteor.*, **13**, 825–830.

- , and W. V. Burt, 1970: Prediction of abnormally heavy precipitation over the equatorial Pacific dry zone. *J. Appl. Meteor.*, **9**, 20–28.
- , and —, 1972: Use of the Southern Oscillation in weather prediction. *J. Appl. Meteor.*, **11**, 616–628.
- Reiter, E. R., 1978a: The interannual variability of the ocean-atmosphere system. *J. Atmos. Sci.*, **35**, 347–370.
- , 1978b: Long-term wind variability in the tropical Pacific, its possible causes and effects. *Mon. Wea. Rev.*, **106**, 324–330.
- Stephens, J. J., and A. L. Polan, 1970: Spectral modification by objective analysis. *Mon. Wea. Rev.*, **99**, 374–378.
- U.S. Navy Hydrographic Office, 1956: *Marine Climatic Atlas of the World*, Vol. II. NAVAER 50-1C-529, 18 pp. + 275 charts.
- Willebrand, J., 1978: Temporal and spatial scales of the wind field over the North Pacific and North Atlantic. *J. Phys. Oceanogr.*, **8**, 1080–1094.
- Wyrski, K., 1975: El Niño—The dynamic response of the equatorial Pacific Ocean to atmospheric forcing. *J. Phys. Oceanogr.*, **5**, 572–584.
- , and G. Meyers, 1975a: The trade wind field over the Pacific Ocean. Part I. The mean field and the mean annual variation. Rep. HIG-75-1, Hawaii Inst. Geophys., University of Hawaii, 26 pp.
- , and —, 1975b: The trade wind field over the Pacific Ocean. Part II. Bimonthly fields of wind stress: 1950 to 1972. Rep. HIG-75-2, Hawaii Inst. Geophys., University of Hawaii, 16 pp.
- , and —, 1976: The trade wind field over the Pacific Ocean. *J. Appl. Meteor.*, **15**, 698–704.
- , E. Stroup, W. Patzert, R. Williams and W. Quinn, 1976: Predicting and observing El Niño. *Science*, **191**, 343–346.